Materials and Design 137 (2018) 463–472

Contents lists available at ScienceDirect

Materials and Design

journal homepage: www.elsevier.com/locate/matdes

Out-of-plane compression of Ti-6Al-4V sandwich panels with corrugated channel cores

Zhen-yu Zhao [a,b], Bin Han [b,c], Xin Wang [a,b], Qian-cheng Zhang [a,b,*], Tian Jian Lu [a,b,*]

[a] State Key Laboratory for Strength and Vibration of Mechanical Structures, Xi'an Jiaotong University, Xi'an 710049, PR China
[b] MOE Key Laboratory for Multifunctional Materials and Structures, Xi'an Jiaotong University, Xi'an 710049, PR China
[c] School of Mechanical Engineering, Xi'an Jiaotong University, Xi'an 710049, PR China

HIGHLIGHTS

- Novel corrugated channel cores are discovered for multifunctional sandwich constructions.
- Corrugated channel cores outperform competing sandwich cores in low density regime.
- Ratio of core web spacing and corrugation amplitude sharply affects compressive response.

GRAPHICAL ABSTRACT

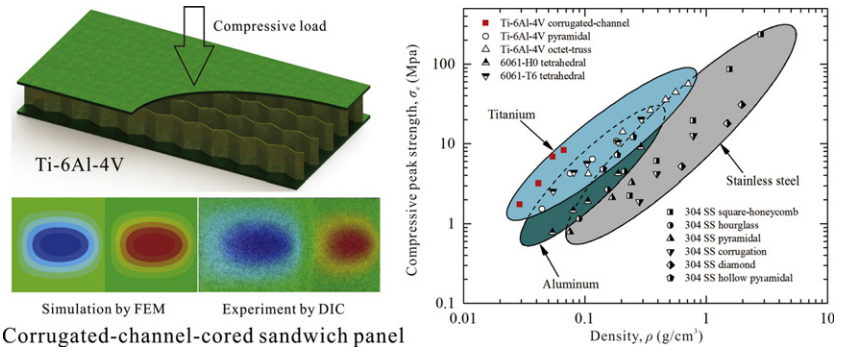

ARTICLE INFO

Article history:
Received 27 June 2017
Received in revised form 17 October 2017
Accepted 19 October 2017
Available online 19 October 2017

Keywords:
Sandwich panel
Titanium alloy
Corrugations
Compressive response
Buckling

ABSTRACT

A novel sandwich core topology – corrugated channels (periodic fluid-through wavy passages) – was proposed for simultaneous load-bearing and active cooling applications. Relative to a sandwich panel with parallel plate channels, the sandwich with corrugated channel core exhibits not only significantly enhanced convective heat transfer rate but also superior mechanical performance. To explore the underlying deformation and failure mechanisms, corrugated-channel-cored sandwich panels (3CSPs) with low relative densities (<1.5%) were manufactured, with Ti-6Al-4V alloy used as the constituent material for both the core and the face sheets. The quasi-static, out-of-plane compressive behaviors of Ti-6Al-4V sandwich panels were systematically studied using a combined experimental, analytical and numerical approach. The compressive strength of the proposed 3CSP was also compared with competing core topologies on the material selection map. With superior structural and thermal efficiency, the corrugated channel core is promising for a wide variety of multifunctional lightweight sandwich constructions.

1. Introduction

Recent developments in all-metallic sandwich constructions have focused not only on searching for even lighter load-bearing structures such as novel periodic lattice cores, but also on pursuing further functionalities such as simultaneous load-bearing and heat dissipation [1]. A variant of lattice cores have thus been proposed to explore such

* Corresponding authors at: State Key Laboratory for Strength and Vibration of Mechanical Structures, Xi'an Jiaotong University, Xi'an 710049, PR China.
E-mail addresses: zqc111999@mail.xjtu.edu.cn (Q. Zhang), tjlu@mail.xjtu.edu.cn (T.J. Lu).

https://doi.org/10.1016/j.matdes.2017.10.055
0264-1275/

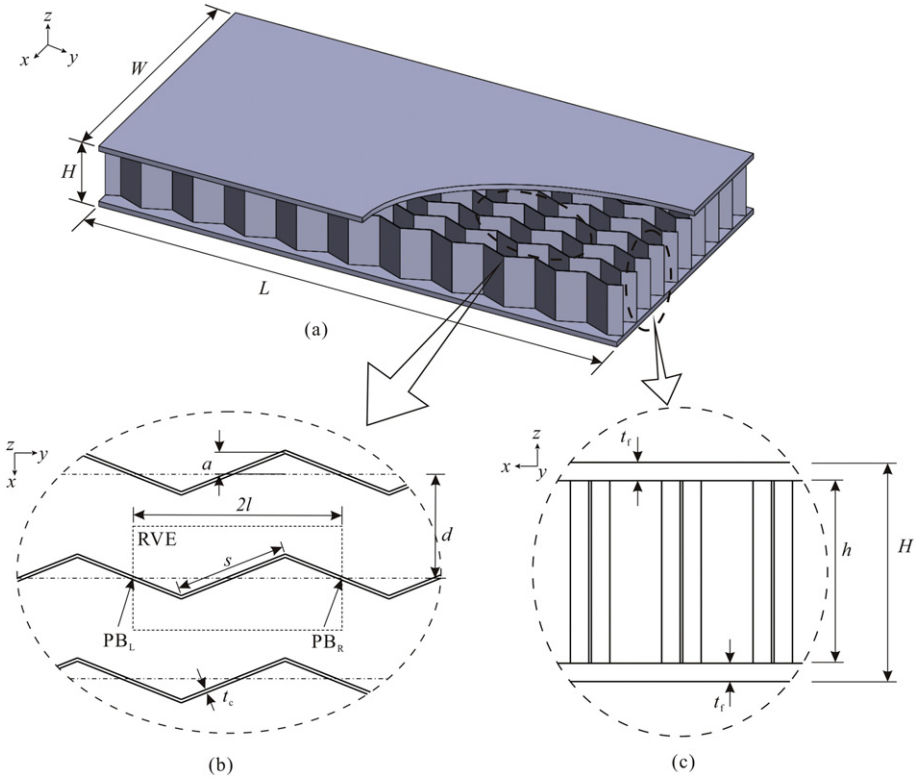

Fig. 1. (a) Schematic of sandwich panel with triangular corrugated channel core; (b) top view and (c) side view. Representative volume element (RVE) with periodic boundary conditions (PB_L and PB_R) for finite element simulation was marked by dashed lines in (b).

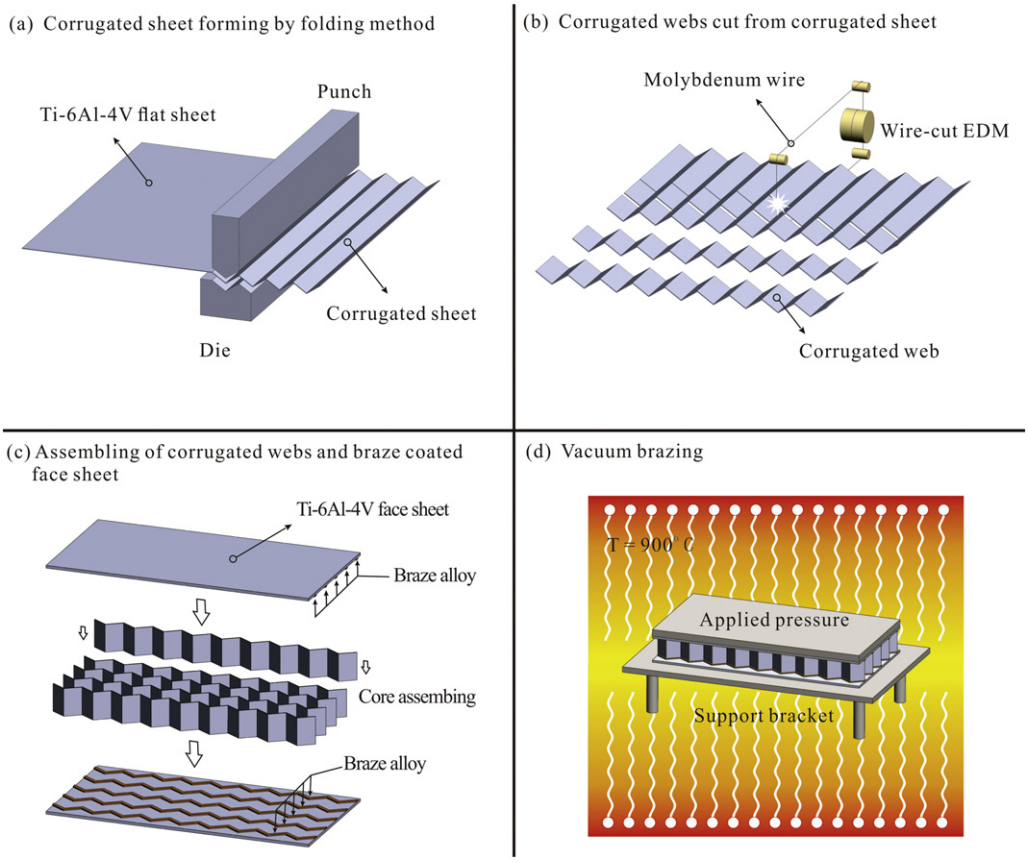

Fig. 2. Fabrication of triangular corrugated-channel-cored sandwich panel: (a) folding of corrugated sheet; (b) fabrication of corrugated web; (c) assembling of sandwich panel; (d) vacuum brazing.

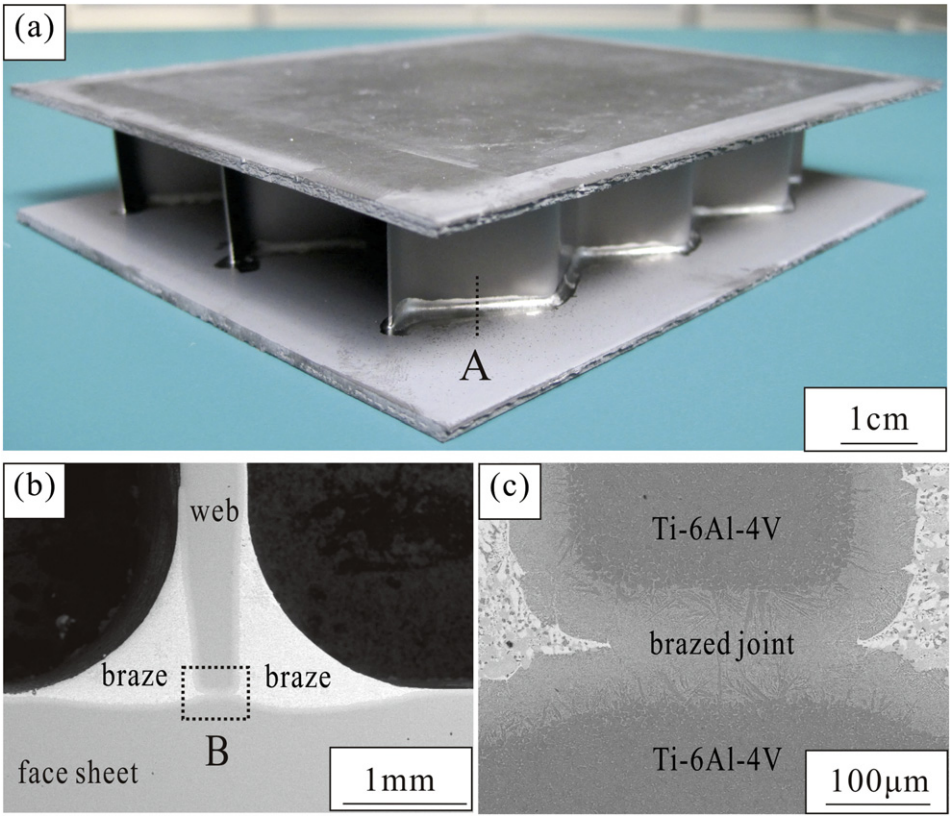

Fig. 3. Images of brazed joint between core web and face sheet: (a) brazed sandwich panel; (b) low magnification view of brazed joint A in (a); (c) high magnification view of brazed gap B in (b).

multi-functionalities as thermal protection, sound insulation and impulsive load mitigation, including square/triangular honeycombs [2,3], corrugations and diamond trusses [4–6], pyramidal and tetrahedral trusses [7–13], X-type trusses [14–16] as well as hybrid cores (e.g., corrugations with either honeycomb or foam insertions) [17–19].

At present, two-dimensional (2D) cellular materials with fluid-through topologies, such as honeycombs and corrugations (folded plates), are perhaps the most prevalent lightweight constructions for multifunctional applications. For instance, Lu [20] developed a modified fin-model to evaluate the efficiency of honeycombs in augmenting the heat transfer performance of compact heat exchangers, and found that the overall heat transfer rate of aluminum honeycombs was comparable to that achieved by open-celled aluminum foams. Subsequently, built upon Lu's analytical solutions, Gu et al. [21] and Wen et al. [22] performed simultaneous evaluation of the structural and heat transfer performances of square, triangular and hexagonal honeycombs. Valdevit et al. [23] used a genetic algorithm to obtain optimal geometric and physical quantities that maximize the active cooling performance of prismatic cored sandwich panels. These sandwich panels were then employed by Valdevit and Vermaak [24,25] to design actively cooled combustion systems of hypersonic vehicles. Similar sandwich structures were also used to construct regenerative cooling systems for the thrust chambers of LOX/Methane liquid rocket engines [26].

Nevertheless, so far as the structural load capacity is of concern, sandwich constructions with fluid-through honeycomb cores were not the best, because the primary function of honeycomb is to carry normal and shear loads perpendicular to the axis of hexagonal/square/triangular prism [27]. For example, Wang and McDowell [28] investigated the in-plane properties of honeycombs with such defects as missing or fractured cell walls using the method of finite elements. The results indicated that the effective elastic stiffness and initial yield strength of honeycombs under in-plane compressive loading were least sensitive to the presence of defects. It has been shown in an experimental investigation by Côté et al. [5] that, under out-of-plane compression loading, prismatic (corrugated and diamond) cores were in weak buckling modes and had lower strength-to-weight ratios than the square-honeycomb core. In order to stabilize the core members against buckling, Yan et al. [19] inserted closed-cell aluminum foams into the interstices of corrugated cores and achieved significantly enhanced peak compressive strength and energy absorption. However, the fluid-through channels of the corrugated cores were blocked by the fillings, the same as honeycomb cores with closed cell topologies (i.e., fluid cannot pass through). Consequently, these cores cannot perform the functionality of active cooling at the same time. To address the deficiency, a new honeycomb core was proposed by truncating the middle portion of the cell walls in a square honeycomb to construct flat heat pipes (sandwich panels) for combined load support and thermal management [29]. Nonetheless, when cell walls are truncated, they buckle more easily under compressive and bend loads especially in the low-density regime of honeycombs.

In the current study, inspired by hexagonal honeycombs fabricated via the sheet crimping process [30], a novel sandwich design with corrugated channel core (corrugated ducts or wavy passages) was proposed, as shown schematically in Fig. 1. From the heat transfer point of view, the enhancement of heat transfer achieved by the corrugated duct could be as large as 2.5 relative to a conventional parallel-plate

Table 1
Geometric details of 3CSP specimens fabricated and tested in the current study.

Specimen no.	Web thickness t_c (mm)	Web height h (mm)	Wave amplitude a (mm)	Length of one-half wave l (mm)	Web spacing d (mm)
1	0.23	22	5	18	40
2	0.33	22	5	18	40
3	0.43	22	5	18	40
4	0.53	22	5	18	40

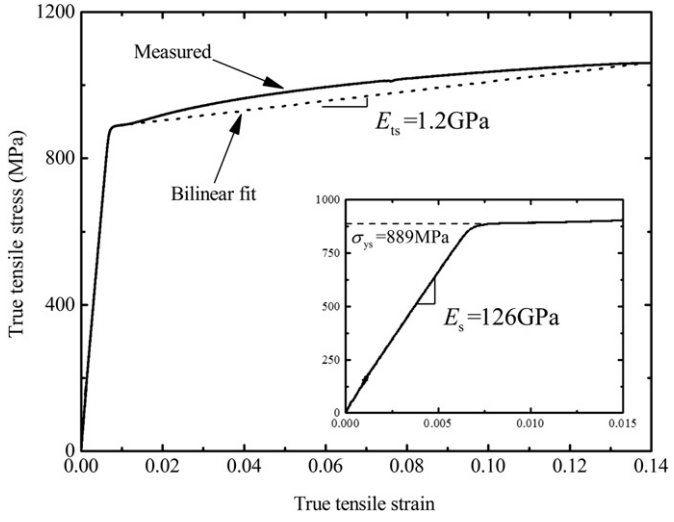

Fig. 4. True tensile stress versus true strain curve of as-brazed Ti-6Al-4V alloy.

channel [31], attractive for applications requiring active cooling as well as load support such as supersonic vehicles, spacecraft skins, acoustic liners and cooling jackets for combustors and jet engines [22,32,33]. While the convective heat transfer characteristics of corrugated channels had been investigated [31], a systematic study on the mechanical performance of corrugated-channel-cored sandwich panels (3CSPs) having corrugated channel cores is yet to be performed. This deficiency is addressed in the current study.

This study aims to investigate the out-of-plane compressive behaviors of 3CSPs using a combined experimental, analytical and numerical approach. The paper is organized as follows. Section 2 presents details concerning the fabrication procedures of Ti-6Al-4V 3CSPs as well as experimental measurements; titanium alloy (Ti-6Al-4V) was selected as the base metal for its high specific yield strength and service temperature [12]. In Section 3, the peak compressive strength of 3CSP was estimated using analytical models of elastic and plastic buckling. To validate the analytical predictions as well as explore deformation modes and failure mechanisms, finite element (FE) simulations were carried out in Section 4. In addition to presenting experimental, analytical and FE results, Section 5 also compared the out-of-plane compressive strength of 3CSPs with competing sandwich core structures on the basis of equal core density.

2. Fabrication and experimental measurement

2.1. Corrugated channel structure

Corrugated-channel-cored sandwich panels with length L, width W and height H, as sketched in Fig. 1a, were manufactured from Ti-6Al-4V alloy (density $\rho_s = 4430$ kg/m^3) sheets and subjected to quasi-static uniform out-of-plane compression. Each sandwich panel was composed of two thin face sheets of equal thickness (t_f) and a corrugated channel core assembled from corrugation webs with thickness t_c and height h. For simplicity, the idealized web profile as shown in Fig. 1b was selected, which presents a triangular corrugation web with wave amplitude a, length of one-half wave l, and hypotenuse length s. The equivalent neutral surfaces of these corrugation webs were parallel to each other with spacing d, and there was no phase shift between the walls (Fig. 1b).

The representative volume element (RVE) with periodic boundary conditions (PB_L and PB_R) for finite element (FE) simulations was marked by dashed lines in Fig. 1b.

The relative density of the triangular corrugated channel core was given by:

$$\overline{\rho} = \sqrt{1 + 4\left(\frac{a}{l}\right)^2}\,\frac{t_c}{d}. \tag{1}$$

2.2. Fabrication methodology

Corrugated channel core sandwich panels were fabricated using a four-step process as shown in Fig. 2. First, Ti-6Al-4V sheet was folded to form triangular corrugations (Fig. 2a). The corrugated sheet was then cut into corrugated webs with wire-cut electro-discharge machining (EDM), as illustrated in Fig. 2b. With reference to Fig. 2c, to create a sandwich panel, vacuum brazing was used to bond the Ti-6Al-4V face sheets and the assembled corrugated core together, as follows: soldering paste with a nominal composition of 40Ti-20Cu-20Ni-20Zr (wt%) (Lucas Milhaupt Co., Ltd) was coated to the contact regions. Upon drying in an oven, the sample was placed in a high–temperature vacuum brazing furnace, which was subsequently evacuated to a base pressure of

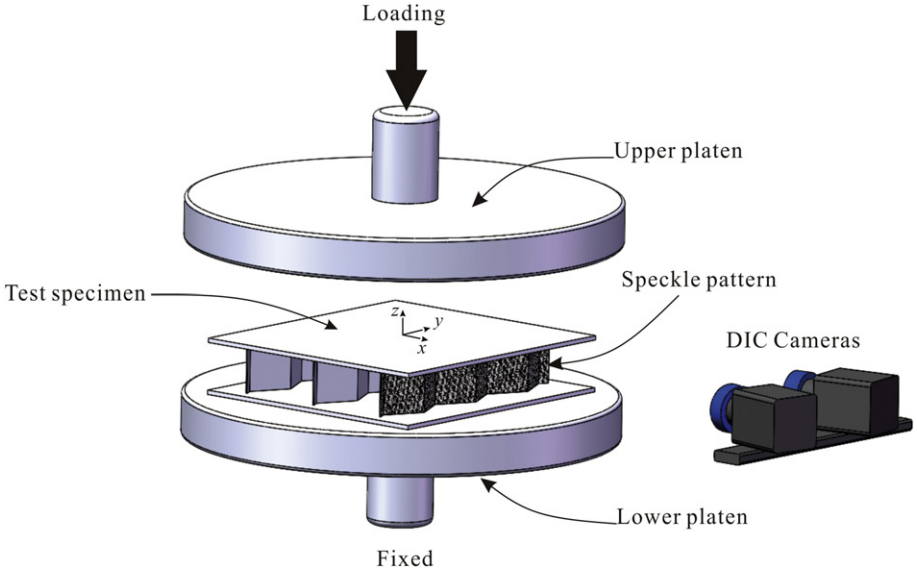

Fig. 5. Schematic of the 3CSP sandwich specimen under out-of-plane compression and the DIC system for surface displacement field measurement. Note that the local coordinate (x, y, z) system was constructed to depict the displacement vector calculated by ARAMIS software.

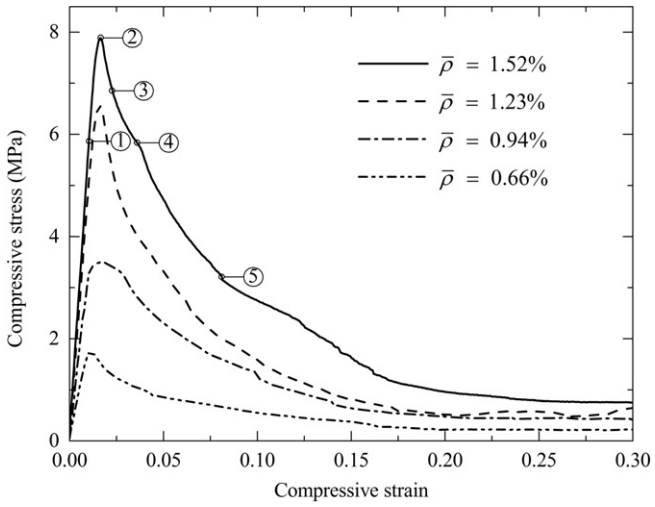

Fig. 6. Nominal compressive stress versus strain responses of Ti-6Al-4V sandwich panels with triangular corrugation channel cores of different relative densities.

~10^{-4} Torr. The sample was heated at the rate of ~10 °C/min to 500 °C and kept at temperature for 20 min to volatilize the polymer binder. Because the solidus and liquidus temperatures of the braze alloy were 848 °C and 856 °C, respectively, and the β-transus temperature for Ti-6Al-4V alloy was 980 °C [10,34], the brazing temperature was set at 900 °C and held for 30 min. After brazing, the furnace was cooled at a rate of ~45 °C/min to 600 °C and annealed for 20 min to minimize residual stresses. Finally, the furnace was cooled to ambient temperature at a rate of ~15 °C/min. Fig. 3a displayed a representative as-brazed sandwich panel.

Table 1 listed the geometric parameters of all the 3CSP specimens tested in the present study, with the face sheet thickness fixed at $t_f = 2$ mm. Note that samples 1 to 4 were different only in the thickness of core webs, and the corresponding relative densities were 0.66%, 0.94, 1.23% and 1.52%.

To assess the quality of the brazed joints, Fig. 3b displayed low magnification image of the interface region marked in Fig. 3a by dashed line A. The Ti-based braze alloy was seen to provide good wettability, forming meniscus-like fillets at the interface between the corrugated web and the face sheet. The gap area between the web and face sheet, marked by dashed box in Fig. 3b, was further magnified under scanning electron microscopy (SEM), as shown in Fig. 3c. The total thickness of the brazed joint gap was about 90 μm The measured shear strength of brazed Ti-6Al-4V joint using the same filler metal as in the current study was approximately 450 MPa [10].

2.3. Mechanical properties of parent material

To characterize the tensile properties of Ti–6Al–4V, dog-bone specimens were cut from as-received Ti-6Al-4V sheet and then subjected to the same thermal history as brazing. Room temperature tensile tests were performed using standard servo-hydraulic test machine (MTS-858 Mini bionix, MTS Corporation, USA), at a nominal strain rate of 1×10^{-3} s^{-1} in accordance with ISO 6892-1:2009 [35]. Load and displacement measurements were provided by the testing

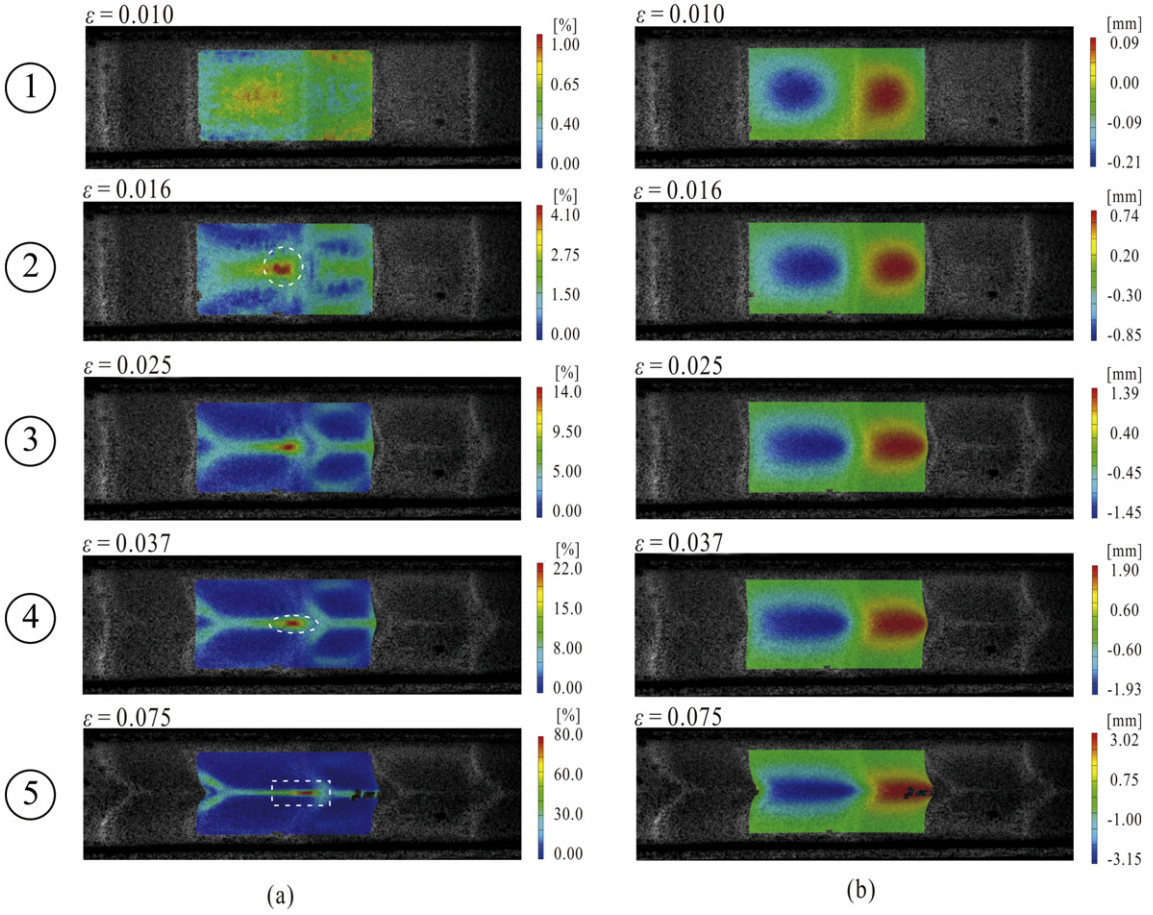

Fig. 7. DIC results for a 3CSP of $\bar{\rho} = 1.52\%$ at Fig. 6 selected strains (a) surface Mises strain; (b) displacement contours on core web surface. Note that the displacement contours were composed of the displacement component along the *x*-axis of the local coordinate shown in Fig. 5.

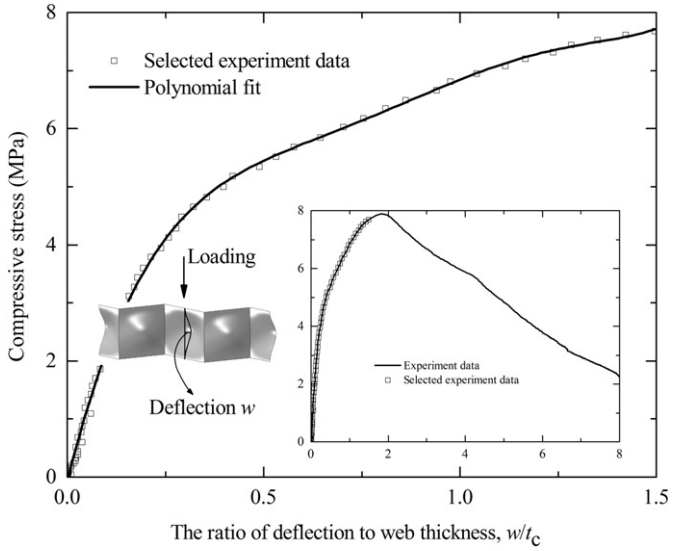

Fig. 8. Measured compressive stress plotted as a function of the ratio of deflection to web thickness ($\overline{\rho} = 1.52\%$).

machine and an extensometer, with an accuracy of 1 N and 10^{-3} mm, respectively.

To determine the Young's modulus E_s and 0.2% offset yield strength σ_{ys}, the measured true tensile stress-strain curve was separated into two parts and fitted using a bi-linear model, as shown in Fig. 4. For the initial linear elastic part, experiment datum on true stresses between 200 and 800 MPa were fitted with a linear equation. The parent material was found to be adequately represented by an elastic-plastic solid of Young's modulus $E_s = 126$ GPa, yield strength $\sigma_{ys} = 889$ MPa and linearly hardening modulus $E_{ts} \approx 1.2$ GPa. The Poisson ratio ν_s was estimated to be 0.34 [36].

2.4. Experimental measurements

3CSP specimens were tested under quasi-static out-of-plane compression following the guidelines of ASTM STP C365 at ambient temperature (25 °C), with a nominal strain rate of 1.67×10^{-4} s^{-1}. Compressive loading was exerted along the *z*-direction (out-of-plane direction) as sketched in Fig. 5. A speckle pattern was applied to the corrugation web surface to collect surface displacement field using a three-dimensional (3D) digital image correlation (DIC) system. The exposed web surface was firstly spray painted white, and then a stochastic pattern of 1–3 mm diameter black dots was employed to cover ~50% of web surface area [37]. To deal with the experimental datum, the reaction force analog signal and the displacement analog signal from the test machine were imported into the DIC system. Upon calibration, images were collected at 2 s intervals during the test. Images of DIC were analyzed using the ARAMIS v6.0.1-3 (GOM mbH, Braunschweig, Germany) software after the test. 15 × 15 pixels facet size and 5 pixels facet spacing were set to calculate the full-field deformation characteristics of the monitored surface as functions of time.

Table 2
Compressive properties of Ti-6Al-4V sandwich panels with corrugated channel cores.

Specimen type	Relative density $\overline{\rho}$ (%)	Compressive stiffness E_c (MPa)	Initial elastic buckling stress σ_c^b (MPa)	Peak stress σ_c^p (MPa)
1	0.66	183.47	0.43	1.75
2	0.94	339.26	1.06	3.5
3	1.23	483.51	4.38	6.56
4	1.52	546.13	5.87	7.89

3. Analytical modeling

3.1. Compressive stiffness

Under out-of-plane compression, the load-carrying capacity of the present corrugation webs was similar to that of hexagonal honeycombs [27] and square honeycombs [38]. Thus, the equivalent compressive modulus E_c of the 3CSP was given by:

$$E_c = \overline{\rho} E_s, \tag{2}$$

where E_s is the Young's modulus of the parent material.

3.2. Out-of-plane compressive strength

The peak out-of-plane compressive strength of Ti-6Al-4V 3CSP was governed by a competition between initial elastic buckling and ultimate buckling of the corrugated webs. Because the corrugated webs were considered to be thin plates, the peak compressive strength of the 3CSP was:

$$\sigma_c = \sigma_{cw} \overline{\rho}, \tag{3}$$

where σ_{cw} is the maximum compressive strength of web walls.

The initial elastic buckling stress was given as [39]:

$$\sigma_{cw}^{eb} = \frac{k\pi^2 E_s}{12(1-\nu_s^2)} \left(\frac{t_c}{s}\right)^2, \tag{4}$$

where $s = \sqrt{4a^2 + l^2}$ and k is a buckling coefficient that depends upon the aspect ratio h/s of web wall (Fig. 1b and c) and the boundary conditions. For a corrugated channel core subjected to simple compression, the two edges perpendicular to the loading direction of each web wall were treated as clamped, while the other two edges parallel to the loading direction were taken as simply supported. For a web wall with aspect ratio $h/s \approx 1$, the buckling coefficient k is approximately equal to 6.74 [40]. Upon substituting Eq. (4) into Eq. (3), the peak compressive strength of the 3CSP induced by elastic buckling is given by:

$$\sigma_c^{eb} = \frac{k\pi^2 E_s}{12(1-\nu_s^2)} \left(\frac{t_c}{s}\right)^2 \overline{\rho}. \tag{5}$$

By substituting $n = d/a$ (n being a scale factor), $s = \sqrt{4a^2 + l^2}$ and Eq. (1) into Eq. (5), a relation between elastic bifurcation stress and core relative density was obtained as:

$$\sigma_c^{eb} = \frac{k\pi^2 E_s}{12(1-\nu_s^2)} \left(\frac{n}{4\xi + 1/\xi}\right)^2 \overline{\rho}^3, \tag{6}$$

where $\xi = a/l$. Alternatively, the non-dimensional elastic buckling stress was given by:

$$\sum\nolimits_c^{eb} = \frac{\sigma_c^{eb}}{\sigma_{ys}\overline{\rho}} = \frac{k\pi^2}{12(1-\nu_s^2)\varepsilon_{ys}} (n\varphi)^2 \overline{\rho}^2 \tag{7}$$

where $\varphi = \frac{1}{4\xi + 1/\xi}$.

The ultimate buckling stress of a rectangular plate was [39]:

$$\sigma_{cw}^{ub} = \frac{\pi}{\sqrt{12(1-\nu_s^2)}} \frac{t_c}{s} \sqrt{kE_s\sigma_{ys}}. \tag{8}$$

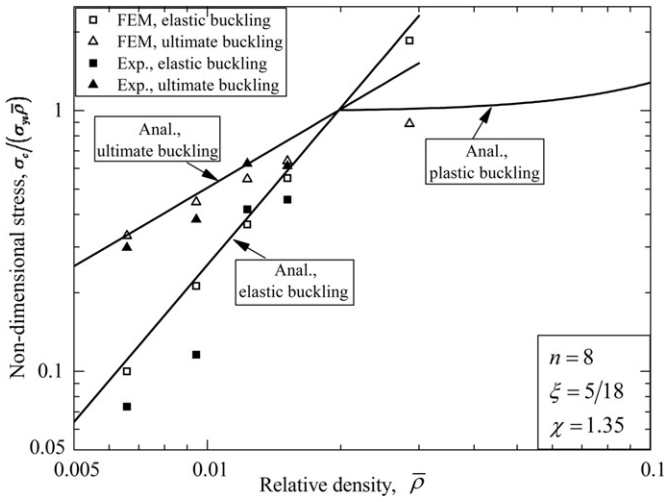

Fig. 9. Analytical predictions of normalized failure stresses with experimental measurements and FE simulation results.

Upon substituting Eq. (8) into Eq. (3), the peak compressive strength of the 3CSP induced by ultimate buckling was obtained as:

$$\sigma_c^{ub} = \frac{\pi}{\sqrt{12(1-\nu_s^2)}}\frac{t_c}{s}\sqrt{kE_s\sigma_{ys}\bar{\rho}}. \tag{9}$$

Again, by substituting $n = d/a, s = \sqrt{4a^2 + l^2}$ and Eq. (1) into Eq. (9), a relation between ultimate buckling stress and core relative density was obtained as:

$$\sigma_c^{eu} = \frac{\pi}{\sqrt{12(1-\nu_s^2)}}\sqrt{kE_s\sigma_{ys}}\frac{n}{4\xi + 1/\xi}\bar{\rho}^2. \tag{10}$$

or, equivalently, as:

$$\sum_c^{eu} = \frac{\sigma_c^{eu}}{\sigma_{ys}\bar{\rho}} = \frac{\pi}{\sqrt{12(1-\nu_s^2)}}\sqrt{\frac{k}{\varepsilon_{ys}}}n\varphi\bar{\rho}, \tag{11}$$

where ε_{ys} is the yield strain of the parent material.

Finally, the plastic buckling stress of a rectangular plate could be expressed as [2]:

$$\sum_c^{p} = \frac{\sigma_c^{p}}{\sigma_{ys}\bar{\rho}} = \frac{\chi\left(\psi\bar{\rho}^2 - 3\varepsilon_{ys}\right) + 3}{\chi\varepsilon_{ys}(2\nu_s - 1) + 3}, \tag{12}$$

where $\chi = E_t/\sigma_{ys}$, $\psi = \frac{k\pi^2}{3}(n\varphi)^2$ and $\varphi = \frac{1}{4\xi + 1/\xi}$.

Table 3
Error analysis between FE simulations and analytical model predictions.

Specimen type	Relative density $\bar{\rho}$ (%)	FE		Anal.		Error	
		EB	UB	EB	UB	For EB	For UB
1	0.66	0.10	0.33	0.11	0.33	−10%	−1%
2	0.94	0.21	0.45	0.23	0.48	−7%	−7%
3	1.23	0.37	0.55	0.39	0.62	−6%	−12%
4	1.52	0.55	0.64	0.59	0.77	−6%	−17%

Note: FE and Anal. refer to finite element calculations and analytically predicted results, respectively, while EB and UB denote the non-dimensional stresses obtained by elastic buckling and ultimate buckling stress, respectively.

4. Finite element simulation

Based on the RVE marked by dashed lines in Fig. 1b, finite element (FE) simulations were carried out using ABAQUS v6.10 (Hibbitt, Karlsson & Sorensen, Inc.). Isotropic hardening was adopted to model Ti-6Al-4V, with Young's modulus $E_s = 126$ GPa, Poisson ratio $\nu_s = 0.34$, and yield stress $\sigma_{ys} = 889$ MPa, as shown in Fig. 4. Corrugated webs were discretized using linear 3D reduced integration shell elements (S4R in ABAQUS notation). Face sheets were modeled as 3D analytical rigid bodies since they were much stiffer than core structures. A mesh refinement study indicated a global element size of 0.5 mm to be sufficient for convergence. Face sheets were assumed to be perfectly bonded with corrugated webs.

An eigenvalue analysis was performed to calculate the initial elastic buckling stresses and capture the buckling modes, while simulation of quasi-static compression was carried out using the explicit solver. The results were all calculated for sandwich panels having imperfections in the form of buckling modes [5]. In this study, an initial imperfection in the shape of the lowest buckling mode, with a peak magnitude 20% of web thickness t_c, was introduced. For periodic boundaries (PB) imposed on the RVE, all the degrees of freedom (both displacements and rotations) of the corresponding pairs of nodes on the left (PB_L) and right (PB_R) boundaries of the RVE (Fig. 1b) were set to the same value [17]. A fixed boundary condition was applied to the bottom face sheet, while through-thickness displacement was uniformly loaded to the top face sheet at a sufficiently low loading rate. In addition, it was established that single-cell, two-cell and even four-cell simulations led to identical results, thus verifying the feasibility of single-cell simulation.

5. Results and discussion

5.1. Experimental results

Fig. 6 presented the measured out-of-plane compressive stress versus strain responses of sandwich samples listed in Table 1. The nominal compressive stress $\sigma_c^n = P/A$ was calculated following ASTM STP C365, where P was the compressive loading and A was the cross-sectional area. These sandwiches exhibited similar compressive behaviors, including an initially linear response region, then a nonlinear response till a peak strength was reached, followed by a sudden and dramatic drop in stress. As expected, the peak strength was strongly dependent upon relative density. The softening after the peak strength was accompanied by large plastic deformation and fracture of core webs, but no breakage of brazed joints occurred during the whole process of compression.

As illustrated, the deformed configurations, surface Mises strain contours and displacement contours corresponding to points ①-⑤ marked in Fig. 6 were shown in Fig. 7 for $\bar{\rho} = 1.52\%$. The deformed configurations of the present triangular corrugated channel core behaved differently from those of traditional corrugated cores [5]: in the former each core web was divided into a plurality of rectangular thin plates and the deformation was governed by the local buckling of these thin plates, while in the latter Euler elastic buckling of constituent struts dominated the deformation [5]. Additional FE simulations results (not shown here for brevity) also confirmed that the two kinds of structures exhibited distinct deformation modes under out-of-plane compression. With reference to Fig. 7b, when the compressive stress reached the initial elastic buckling stress, as shown in image ①, the central part of the rectangular thin plates bulged out distinctly. When the stress was increased to the peak stress at $\varepsilon = 1.6\%$ in configuration ②, there was a Mises strain concentration region, marked in Fig. 7a by dashed circle line and the folding lines (i.e., the supported edges of rectangular plates) experienced bending, followed by structural instability. At configuration ③, the surface Mises strain reached the tensile elongation limit (~14%; Fig. 4) of Ti-6Al-4V, accompanied by a noticeably audible cracking noise. As the

Table 4
Error analysis between experimental results and analytical model predictions.

Specimen type	Relative density $\bar{\rho}$ (%)	Exp.		Anal.		Error	
		EB	UB	EB	UB	For EB	For UB
1	0.66	0.07	0.30	0.11	0.33	−34%	−10%
2	0.94	0.12	0.38	0.23	0.48	−49%	−20%
3	1.23	0.42	0.63	0.39	0.62	7.7%	0.5%
4	1.52	0.46	0.61	0.59	0.77	−23%	−20%

Note: Exp. and Anal. refer to experimental and analytically predicted results, respectively, while EB and UB denote the non-dimensional stresses obtained by elastic buckling and ultimate buckling stress, respectively.

compressive stressing was further increased, small fractures in configuration ④ became linear fractures in configuration ⑤, as marked by dashed ellipse and rectangle lines in Fig. 7a, respectively.

To determine the initial elastic buckling stress, Fig. 8 plotted the measured compressive stress as a function of the ratio of deflection w to web thickness t_c, which resembled the typical response of a simply supported plate subjected to uniform compressive edge loading. The deflection w in the geometric center of a single rectangular plate was calculated by x-direction displacement derived using the ARAMIS software and the included angle between the x-direction shown in Fig. 5 and the normal direction of the web. Selected experiment data were intercepted from the overall data shown in the inset. The 6th order polynomial fitting (solid line) for the selected data was employed according to the inflection point method on load-deflection curve [41], yielding:

$$\sigma_c^n = 2.279(w/t_c)^6 - 3.0214(w/t_c)^5 - 17.741(w/t_c)^4 + 51.255(w/t_c)^3 - 52.804(w/t_c)^2 + 26.933(w/t_c) - 0.058 \tag{13}$$

The curve's coefficient of determination (R^2) was 0.9987.

To find the inflection point, the minimal root obtained by equating the second derivative of Eq. (13) to zero was applied to determine the initial elastic buckling stress. The corresponding results were summarized in Table 2.

5.2. Comparison of analytical predictions with experimental measurements and FE calculations

Fig. 9 compared the analytically predicted elastic buckling and ultimate buckling stresses with the experimental measurements with $\varepsilon_{ys} = 0.7\%$, $\chi = 1.35$, $n = 8$ and $\xi = 5/18$ for selected values of relative density ($\bar{\rho}$). Overall, reasonable agreement was achieved.

Table 3 summarized the data used to plot Fig. 9 and the relative errors between FE simulations and analytical predictions. Note that the elastic buckling stress by FE was calculated using buckle analysis in linear perturbation steps. The error analysis showed that the FE simulation results were slightly smaller than the analytical predictions: while the errors for elastic buckling were relatively constant (−7%), the errors for ultimate buckling increased from −1% to −17% as the relative density was increased. The difference was mainly attributed to the difference in the way the connection nodes between core webs and face sheets was modeled: the two edges perpendicular to the loading direction of each web wall were taken as clamped in analytical modeling, but not strictly treated as clamped in FE simulation.

Error analysis between experimental results and analytical predictions was also carried out, as shown in Table 4. Due to processing-induced imperfections in corrugated channel cores, the relative errors between experiment and analytical modeling for elastic buckling were obvious, especially when the relative density was low. The thinner the core webs were, the harder it was to control the geometric defects. Whereas, the errors for ultimate buckling were acceptable. This implied that the results of ultimate buckling stress for 3CSPs were relatively less sensitive to the presence of geometric imperfections.

To validate the analytical prediction further, FE calculation results for a specimen with $\bar{\rho} = 0.029$ were also shown in Fig. 9. These results demonstrated that both the elastic buckling and plastic buckling stresses were in agreement with the present analytical predictions.

5.3. Effect of non-dimensional geometric parameters ξ and n

From Eqs. (11) and (12), it could be concluded that the non-dimensional peak stresses of 3CSPs under compression were dependent upon the topological core parameters $\bar{\rho}$, k, $\xi = a/l$ and $n = d/a$, and parent material properties, such as the yield strain ε_{ys}, $\chi = E_t/\sigma_{ys}$ and ν_s. In Eqs. (11) and (12), it was assumed that:

$$\varphi = \frac{1}{4\xi + 1/\xi}. \tag{14}$$

It followed that $\varphi_{max} = 1/4$ when $\xi = 1/2$.

For applications of simultaneous load-bearing and active cooling, the non-dimensional geometrical parameter $n = d/a$ not only played an important role at low Reynolds numbers but also governed the stability of corrugated channels [42]. In Fig. 10, the peak failure stress of 3CSPs predicted using Eqs. (11) and (12) was plotted as function of relative density for selected values of d/a, with $\xi = 1/2$, $\chi = 1.35$ and $\varepsilon_{ys} = 0.7\%$. The peak stress was significantly affected by d/a and the predicted transition of relative density from ultimate buckling stress to plastic buckling stress decreased with increasing d/a.

5.4. Comparison of competing topologies

To compare the proposed corrugated channel cores with competing sandwich core topologies under out-of-plane compression, Fig. 11 plotted the experimentally measured peak compressive strengths σ_c as functions of core density ρ. In addition to Ti-6Al-4V alloy used in the current study, the parent materials compared include 304 stainless steel (square-honeycombs [2], corrugated cores [5], diamond cores [5], hourglass trusses [9], pyramidal trusses [9] and hollow pyramidal trusses [7]), aluminum alloy (tetrahedral trusses [43]), and titanium alloy (pyramidal trusses [12] and octet-trusses [10]). As titanium alloy has a higher specific strength than the other metallic materials, the topologies made from it were seen to be stronger on a per weight basis

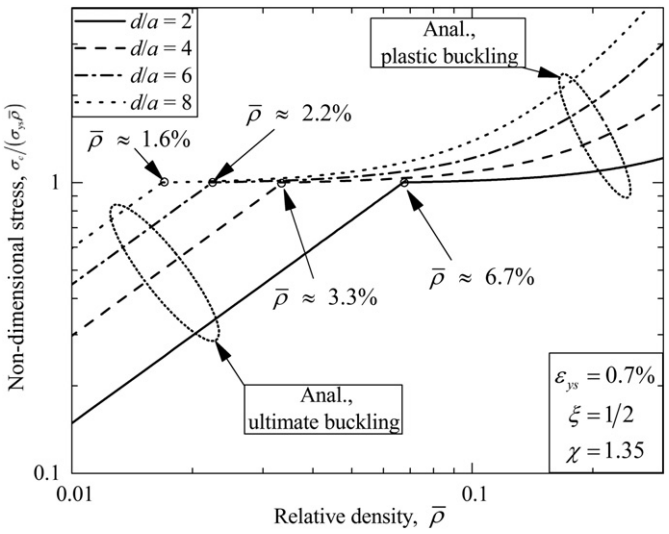

Fig. 10. Analytically predicted peak failure stress plotted as a function of relative density for selected values of d/a.

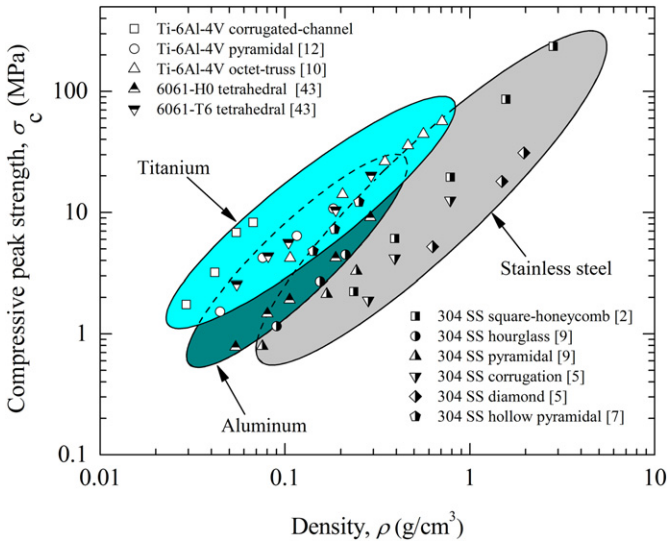

Fig. 11. Comparison of experimentally measured peak compressive strengths of competing sandwich core topologies.

in general. In particular, in the low density regime, the corrugated channel cores made of Ti-6Al-4V exhibited obvious superiority than those made by the same parent material, e.g., pyramidal trusses [12] and octet-trusses [10].

To further demonstrate the superiority of corrugated channel structure, the non-dimensional compressive strengths ($\sigma_c/\sigma_{ys}\bar{\rho}$) of the 3CSPs predicted analytically with $\xi = 1/2$ and $n = 8$ were compared with those of competing lattices in Fig. 12, including square honeycombs [2], corrugated cores [5], pyramidal trusses [9] and hollow pyramidal trusses [7]. In the analytical modeling, the sandwich core structures were all assumed to be made from an elastic-ideally plastic solid with yield strain $\varepsilon_{ys} = 0.7\%$. Analytical predictions of typical lattice cores were reviewed by Kooistra et al. [44]. For hollow pyramidal trusses, there existed no explicit relationship between the compressive strength and relative density, and hence the sequential quadratic programming (SQP) algorithm was used to calculate the peak failure stress.

From Fig. 12 it was seen that, within the range of relative density considered, almost all the ultra-lightweight sandwich cores collapsed by elastic buckling first and then yielding, except for hollow pyramidal trusses. The non-dimensional failure stress of an optimized hollow

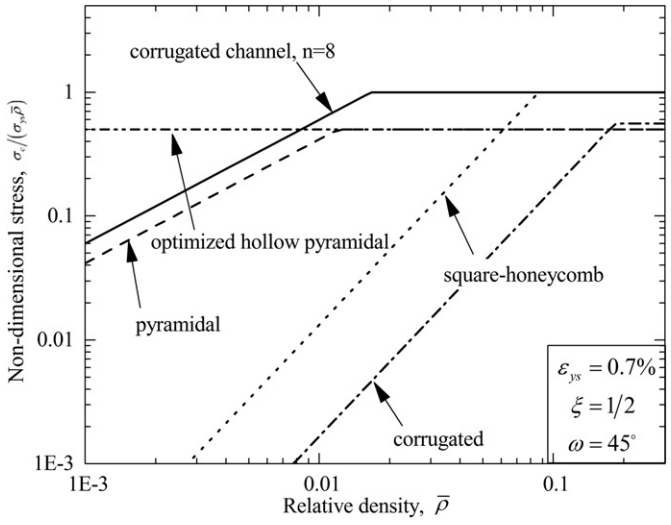

Fig. 12. Analytically predicted failure stresses of competing sandwich cores plotted as functions of relative density.

pyramidal truss was given by the yielding stress of hollow truss and equal to its optimal value of 0.5. In the region of $0.008<\bar{\rho}<0.08$, the corrugated channel core outperformed all the other lattice cores. However, for very low relative densities ($\bar{\rho}<0.008$), the optimized hollow pyramidal truss exhibited the best performance. Surprisingly, for $\bar{\rho}>0.08$, the corrugated channel core had the same non-dimensional failure stress as the square honeycomb, for they both collapsed by yielding (core members aligned with the loading direction). However, with fluid-through passages, corrugated channel cores enabled simultaneous load-bearing and active cooling, while square honeycombs could not be used for such multifunctional applications.

6. Conclusions

Ultra-lightweight corrugated-channel-cored sandwich panels (3CSPs) made of Ti-6Al-4V were manufactured via vacuum brazing. Quasi-static, out-of-plane compressive behavior of the 3CSP was investigated using a combined approach of experimental measurement, analytical modeling and numerical simulation. Analytical predictions based upon thin plate buckling theory agreed reasonably well with experimental measurements and numerical calculations. Compared with competing sandwich core topologies such as square honeycombs, hollow pyramidal trusses and octet trusses, the proposed corrugated channel core exhibited superiority particularly in the low density regime. The 3CSPs hold great potential for applications requiring simultaneous load support and active cooling at low weight.

Acknowledgements

This work was supported by the National Natural Science Foundation of China (11472209, and 11472208), China Postdoctoral Science Foundation (2016M600782), Postdoctoral Scientific Research Project of Shaanxi Province (2016BSHYDZZ18), the Fundamental Research Funds for Xian Jiaotong University (xjj2015102) and Jiangsu Province Key Laboratory of High-end Structural Materials (hsm1305). Z.Y. Zhao wished to thank Drs. B. Yu and H.B. Yan for insightful discussions.

References

[1] Q.C. Zhang, X.H. Yang, P. Li, G.Y. Huang, S.S. Feng, C. Shen, et al., Bioinspired engineering of honeycomb structure – using nature to inspire human innovation, Prog. Mater. Sci. 74 (2015) 332–400.
[2] F. Côté, V.S. Deshpande, N.A. Fleck, A.G. Evans, The out-of-plane compressive behavior of metallic honeycombs, Mater. Sci. Eng. A 380 (2004) 272–280.
[3] F.W. Zok, H. Rathbun, M.Y. He, E. Ferri, C. Mercer, R.M. McMeeking, et al., Structural performance of metallic sandwich panels with square honeycomb cores, Philos. Mag. 85 (2005) 3207–3234.
[4] L. Valdevit, Z. Wei, C. Mercer, F.W. Zok, A.G. Evans, Structural performance of near-optimal sandwich panels with corrugated cores, Int. J. Solids Struct. 43 (2006) 4888–4905.
[5] F. Côté, V.S. Deshpande, N.A. Fleck, A.G. Evans, The compressive and shear responses of corrugated and diamond lattice materials, Int. J. Solids Struct. 43 (2006) 6220–6242.
[6] L. Valdevit, J.W. Hutchinson, A.G. Evans, Structurally optimized sandwich panels with prismatic cores, Int. J. Solids Struct. 41 (2004) 5105–5124.
[7] D.T. Queheillalt, H.N.G. Wadley, Pyramidal lattice truss structures with hollow trusses, Mater. Sci. Eng. A 397 (2005) 132–137.
[8] H.J. Rathbun, Z. Wei, M.Y. He, F.W. Zok, A.G. Evans, D.J. Sypeck, et al., Measurement and simulation of the performance of a lightweight metallic sandwich structure with a tetrahedral truss core, J. Appl. Mech. 71 (2004) 368.
[9] L.J. Feng, L.Z. Wu, G.C. Yu, An hourglass truss lattice structure and its mechanical performances, Mater. Des. 99 (2016) 581–591.
[10] L. Dong, V. Deshpande, H. Wadley, Mechanical response of Ti–6Al–4V octet-truss lattice structures, Int. J. Solids Struct. 60–61 (2015) 107–124.
[11] P. Moongkhamklang, V.S. Deshpande, H.N.G. Wadley, The compressive and shear response of titanium matrix composite lattice structures, Acta Mater. 58 (2010) 2822–2835.
[12] D.T. Queheillalt, H.N.G. Wadley, Titanium alloy lattice truss structures, Mater. Des. 30 (2009) 1966–1975.
[13] C. Shen, Q.C. Zhang, S.Q. Chen, H.Y. Xia, F. Jin, Sound transmission loss of adhesively bonded sandwich panels with pyramidal truss core: theory and experiment, Int. J. Appl. Mech. 7 (2015) 1550013.

[14] Q.C. Zhang, Y.J. Han, C.Q. Chen, T.J. Lu, Ultralight X-type lattice sandwich structure (I): concept, fabrication and experimental characterization, SCIENCE CHINA Technol. Sci. 52 (2009) 2147–2154.
[15] Q.C. Zhang, A.P. Chen, C.Q. Chen, Ultralight X-type lattice sandwich structure (II): micromechanics modeling and finite element analysis, SCIENCE CHINA Technol. Sci. 52 (2009) 2670–2680.
[16] H.B. Yan, Q.C. Zhang, T.J. Lu, Heat transfer enhancement by X-type lattice in ventilated brake disc, Int. J. Therm. Sci. 107 (2016) 39–55.
[17] B. Han, K.K. Qin, B. Yu, B. Wang, Q.C. Zhang, T.J. Lu, Honeycomb–corrugation hybrid as a novel sandwich core for significantly enhanced compressive performance, Mater. Des. 93 (2016) 271–282.
[18] B. Han, K.K. Qin, B. Yu, Q.C. Zhang, C.Q. Chen, T.J. Lu, Design optimization of foam-reinforced corrugated sandwich beams, Compos. Struct. 130 (2015) 51–62.
[19] L.L. Yan, B. Yu, B. Han, C.Q. Chen, Q.C. Zhang, T.J. Lu, Compressive strength and energy absorption of sandwich panels with aluminum foam-filled corrugated cores, Compos. Sci. Technol. 86 (2013) 142–148.
[20] T.J. Lu, Heat transfer efficiency of metal honeycombs, Int. J. Heat Mass Transf. 42 (1999) 2031–2040.
[21] S. Gu, T.J. Lu, A.G. Evans, On the design of two-dimensional cellular metals for combined heat dissipation and structural load capacity, Int. J. Heat Mass Transf. 44 (2001) 2163–2175.
[22] T. Wen, J. Tian, T.J. Lu, D.T. Queheillalt, H.N.G. Wadley, Forced convection in metallic honeycomb structures, Int. J. Heat Mass Transf. 49 (2006) 3313–3324.
[23] L. Valdevit, A. Pantano, H.A. Stone, A.G. Evans, Optimal active cooling performance of metallic sandwich panels with prismatic cores, Int. J. Heat Mass Transf. 49 (2006) 3819–3830.
[24] L. Valdevit, N. Vermaak, F.W. Zok, A.G. Evans, A materials selection protocol for lightweight actively cooled panels, J. Appl. Mech. 75 (2008), 061022. .
[25] N. Vermaak, L. Valdevit, A.G. Evans, F.W. Zok, R.M. Mcmeeking, Implications of shakedown for design of actively cooled thermostructural panels, J. Mech. Mater. Struct. 6 (2012) 1313–1327.
[26] J. Song, B. Sun, Thermal-structural analysis of regeneratively-cooled thrust chamber wall in reusable LOX/Methane rocket engines, Chin. J. Aeronaut. 30 (2017) 1043–1053.
[27] J. Zhang, M.F. Ashby, The out-of-plane properties of honeycombs, Int. J. Mech. Sci. 34 (1992) 475–489.
[28] A.J. Wang, D.L. Mcdowell, Effects of defects on in-plane properties of periodic metal honeycombs, Int. J. Mech. Sci. 45 (2003) 1799–1813.
[29] D.T. Queheillalt, G. Carbajal, G.P. Peterson, Wadley HNG, A multifunctional heat pipe sandwich panel structure, Int. J. Heat Mass Transf. 51 (2008) 312–326.
[30] H. Wadley, Fabrication and structural performance of periodic cellular metal sandwich structures, Compos. Sci. Technol. 63 (2003) 2331–2343.
[31] G. Wang, S.P. Vanka, Convective heat transfer in periodic wavy passages, Int. J. Heat Mass Transf. 38 (1995) 3219–3230.
[32] X.C. Xue, Yu YG, Q. Zhang, Study on the influences of interaction behaviors between multiple combustion-gas jets on expansion characteristics of Taylor cavities, Acta Mech. Sinica 31 (2015) 720–731.
[33] L. Tian, L.H. Chen, Q. Chen, F.Q. Zhong, X.Y. Chang, Engine performance analysis and optimization of a dual-mode scramjet with varied inlet conditions, Acta Mech. Sinica 32 (2016) 75–82.
[34] M.J. Donachie, Titanium: A Technical Guide, ASM International, 2000.
[35] ISO 6892-1, Metallic Materials-Tensile Testing-Part 1: Method of Test at Room Temperature, ISO, 2009.
[36] T. Tancogne-Dejean, C.C. Roth, U. Woy, D. Mohr, Probabilistic fracture of Ti–6Al–4V made through additive layer manufacturing, Int. J. Plast. 78 (2016) 145–172.
[37] M.R. O'Masta, B.G. Compton, E.A. Gamble, F.W. Zok, V.S. Deshpande, H.N.G. Wadley, Ballistic impact response of an UHMWPE fiber reinforced laminate encasing of an aluminum-alumina hybrid panel, Int. J. Impact Eng. 86 (2015) 131–144.
[38] B. Russell, V. Deshpande, H. Wadley, B. Russell, H. Wadley, Quasistatic deformation and failure modes of composite square honeycombs, J. Mech. Mater. Struct. 3 (2008) 1315–1340.
[39] S.P. Timoshenko, J.M. Gere, W. Prager, Theory of elastic stability, J. Appl. Mech. 29 (1962) 220.
[40] E. Ventsel, T. Krauthammer, Thin Plates and Shells: Theory: Analysis, and Applications, CRC Press, 2001.
[41] M. Paszkiewicz, T. Kubiak, Selected problems concerning determination of the buckling load of channel section beams and columns, Thin-Walled Struct. 93 (2015) 112–121.
[42] T.A. Rush, T.A. Newell, A.M. Jacobi, An experimental study of flow and heat transfer in sinusoidal wavy passages, Int. J. Heat Mass Transf. 42 (1999) 1541–1553.
[43] G.W. Kooistra, V.S. Deshpande, H.N.G. Wadley, Compressive behavior of age hardenable tetrahedral lattice truss structures made from aluminium, Acta Mater. 52 (2004) 4229–4237.
[44] G.W. Kooistra, V.S. Deshpande, H.N.G. Wadley, Hierarchical corrugated core sandwich panel concepts, J. Appl. Mech. 74 (2005) 259–268.